



## Full Length Article

# TiCrNb hydride fabricated by melt spinning as the efficient catalyst for enhancing the hydrogen storage properties of MgH<sub>2</sub>

Houqun Xiao<sup>a,b,#</sup>, Luocai Yi<sup>a,#</sup>, Huxu Lei<sup>a</sup>, Yu Xu<sup>a</sup>, Xiaoxuan Zhang<sup>a</sup>, Huazhou Hu<sup>a</sup>, Ruizhu Tang<sup>a</sup>, Qian Li<sup>c,\*</sup>, Qingjun Chen<sup>a,\*</sup>

<sup>a</sup>Key Laboratory of Rare Earths, Jiangxi Institute of Rare Earths, Ganjiang Innovation Academy, Chinese Academy of Sciences, Ganzhou, 341000, China

<sup>b</sup>School of Intelligent Manufacturing and Materials Engineering, Gannan University of Science and Technology, Ganzhou 341000, China

<sup>c</sup>National Engineering Research Center for Magnesium Alloys, College of Materials Science and Engineering, Chongqing University, Chongqing 400044, China

Received 18 October 2024; received in revised form 26 December 2024; accepted 7 January 2025

Available online xxx

## Abstract

Magnesium hydride (MgH<sub>2</sub>) has garnered significant attention as a promising material for high-capacity hydrogen storage. However, its commercial application remains challenging due to the high operating temperature and slow reaction kinetics. In this study, melt-spun Ti<sub>45</sub>Cr<sub>40</sub>Nb<sub>15</sub> (with a BCC phase) hydride (designated as TiCrNbH<sub>x</sub>-MS) was synthesized and used to form a nano-multiphase composite to improve the de-/rehydrogenation properties of MgH<sub>2</sub> through ball milling. The incorporation of TiCrNbH<sub>x</sub>-MS was shown to significantly enhance the hydrogen de-/rehydrogenation properties of MgH<sub>2</sub>. The MgH<sub>2</sub> + 20 wt% TiCrNbH<sub>x</sub>-MS composite exhibits an appealing initial dehydrogenation temperature of 163 °C and can absorb hydrogen at room temperature. Notably, it releases 5.8 wt% hydrogen in 700 s at 230 °C and recharges 4.3 wt% hydrogen in just 2 mins at 150 °C. Even after 100 cycles, it retains a reversible hydrogen capacity of 4.98 wt%. Kinetic analysis revealed that the dehydrogenation rate follows the Chou surface penetration model. Microstructural analysis showed that the FCC phase of the melt-spun TiCrNbH<sub>x</sub>-MS hydride reversibly transformed into the BCC phase during the de-/rehydrogenation process in the composite. Numerous phase interfaces were generated and uniformly dispersed on the MgH<sub>2</sub> surface, providing additional hydrogen diffusion pathways and heterogeneous nucleation sites for Mg/MgH<sub>2</sub>, thereby further improving the hydrogen de-/rehydrogenation kinetics of the system. This study offers valuable insights into the use of multiphase composites to enhance MgH<sub>2</sub> performance.

© 2025 Chongqing University. Publishing services provided by Elsevier B.V. on behalf of KeAi Communications Co. Ltd.

This is an open access article under the CC BY license (<http://creativecommons.org/licenses/by/4.0/>)

Peer review under responsibility of Chongqing University

**Keywords:** MgH<sub>2</sub>; BCC; Hydrogen storage; Structural evolution; Multiphasic composite.

## 1. Introduction

Hydrogen, the simplest element in the periodic table, has increasingly emerged as a key component in addressing the complex challenges of climate change and the energy crisis. The global consensus is to develop hydrogen energy as part of efforts to reduce carbon emissions and achieve energy

transformation [1,2]. However, finding a low-cost, efficient, reversible, and safe method for hydrogen storage remains critical to the advancement of the hydrogen economy [3,4]. Compared to storing hydrogen in its gaseous form, which requires significant compression, or in liquid form, which necessitates cooling to below -253 °C, solid-state hydrogen storage offers greater potential in terms of safety and energy efficiency [5–7]. Early hydrogen storage materials, such as LaNi<sub>5</sub>, TiMn<sub>2</sub>, and TiFe, could readily and reversibly absorb and release hydrogen under moderate conditions after full activation. However, their low hydrogen storage capacities (1.4–2.0 wt%) limit their practical application [8–10]. Magnesium hydride (MgH<sub>2</sub>), by contrast, has attracted more

\* Corresponding author at: Key Laboratory of Rare Earths, Jiangxi Institute of Rare Earths, Ganjiang Innovation Academy, Chinese Academy of Sciences, Ganzhou, 341000, China.

E-mail addresses: [cqliqian@cqu.edu.cn](mailto:cqliqian@cqu.edu.cn) (Q. Li), [qjchen@gia.cas.cn](mailto:qjchen@gia.cas.cn) (Q. Chen).

# These authors contributed equally to this work.

attention due to its high hydrogen storage capacity (7.6 wt%), along with the abundance and low cost of magnesium [11,12]. Despite these advantages, the high operating temperature required for dehydrogenation ( $> 300^{\circ}\text{C}$ ) and the slow hydrogen de-/rehydrogenation rates have hindered its large-scale industrial use [13,14]. To overcome these challenges, a range of modification strategies, such as alloying, catalyst doping, nanosizing, and compositing, have been widely explored to improve the thermodynamics and kinetics of hydrogen de-/rehydrogenation in Mg/MgH<sub>2</sub> systems [15–20].

It is worth noting that catalytic doping has been proven to be one of the most practical and effective methods for enhancing the de-/rehydrogenation properties of MgH<sub>2</sub> [21–23]. Multivalent transition metals (TMs) and their compounds have been extensively studied for their ability to accelerate the breaking and recombination of Mg-H and H-H bonds. This enhancement is attributed to the unsaturated D-band electrons of TMs, which cause greater perturbation compared to Mg when interacting with the hydrogen antibonding orbitals [24]. Cui et al. [25] demonstrated closed correlation on the electronegativities of TMs against the dehydrogenation of MgH<sub>2</sub>, ranking from Ti, Nb, Ni, V, Co to Mo. Zhang et al. [26] employed the synthesized multivalent NbH<sub>x</sub>, ball milled with MgH<sub>2</sub>, and achieved 7 wt% of hydrogen dehydrogenation within 9 mins upon 3 kPa at 300 °C. Jangir et al. [27] adopted 5 wt% TiH<sub>2</sub> doped into MgH<sub>2</sub> and the composites exhibited a much lower dehydrogenated activation energy ( $-77.56\text{ kJ/mol}$ ) than the pristine MgH<sub>2</sub> ( $-137.13\text{ kJ/mol}$ ). Dan et al. [28] developed Nb-doped TiO<sub>2</sub> for MgH<sub>2</sub>, and achieved that 6 wt% H<sub>2</sub> releasing in 12 mins at 225 °C and 5 wt% H<sub>2</sub> absorbing for 20 s at room temperature when incorporated 8 wt% Ti(30Nb)O<sub>2</sub> to MgH<sub>2</sub>. Liu et al. [29] synthesized a novel nanosized NiCoFeCuMg HEA@C catalysts modified MgH<sub>2</sub>, and achieved an initial dehydrogenation temperature down to 167.2 °C, accompanied by a stable 97 % reversible hydrogen capacity retention over 20 cycles.

Additionally, intermetallic compounds of multivalent transition metals (TMs), such as TiAl, Ti<sub>3</sub>Al, TiV, TiNb, ZrMn<sub>2</sub>, LaNi<sub>5</sub>, and TiCrV, have gained significant attention due to their synergistic catalytic effects [30–33]. A particularly favoured approach involves doping intrinsic hydrogen storage compounds like TiFe [34], LaNi<sub>5</sub> [10], V-based solid solution [35] into the Mg/MgH<sub>2</sub> system, capitalizing on the strengths of each component. This method not only harnesses synergistic catalytic effects but also maintains the system's higher hydrogen storage capacity, avoiding the added weight associated with conventional catalysts.

For instance, Lu et al. [36] prepared a composite of MgH<sub>2</sub> doped with 10 wt% TiFe and 5 wt% CNTs, which released 6.5 wt% hydrogen in 10 mins at 300 °C and reabsorbed 5.3 wt% H<sub>2</sub> at 125 °C under 3 MPa pressure. Liang et al. [37] demonstrated excellent low-temperature hydrogenation kinetics in Mg + 50 at% LaNi<sub>5</sub> composites, prepared via mechanical milling under an Ar atmosphere. The enhanced performance was attributed to numerous phase boundaries and porous surfaces formed during the de-/rehydrogenation process, particularly the phases Mg, LaH<sub>x</sub>, and Mg<sub>2</sub>Ni.

Moreover, V-based BCC-type hydrogen storage alloys, which offer a capacity of approximately 4.0 wt% H<sub>2</sub>, have been widely introduced to modify MgH<sub>2</sub>, significantly improving both the de-/rehydrogenation properties and cyclic performance of Mg/MgH<sub>2</sub> systems. For example, Yu et al. [38] showed that the hydride of TiCrVMn BCC alloys catalyzed MgH<sub>2</sub>, releasing 5.7 wt% hydrogen in 30 mins at 290 °C and reabsorbing over 90 % of the initial hydrogen capacity within 100 mins at 100 °C. This improvement was attributed to the increased hydrogen diffusion channels provided by micro- and nanosized particles and defects in the nano or amorphous phases on the MgH<sub>2</sub> surface. Similarly, Zhang et al. [39] utilized nanocrystalline Mg-20 wt% Ti<sub>0.16</sub>Cr<sub>0.24</sub>V<sub>0.6</sub> composites via reactive ball milling, achieving 5.67 wt% hydrogen dehydrogenation in 20 mins at 270 °C and 0.01 MPa.

However, V-based BCC type alloys are costly due to the high price and challenging smelting process of V raw materials. To address this, recent developments have focused on low-V or V-free BCC-type alloys to reduce costs. Researchers have successfully substituted V with Fe or Mo, achieving reasonable hydrogen storage properties in these alloys [40]. Our group has also developed economical V-free BCC-type alloys with a single BCC phase, using Nb or Mo as substitutes for V through rapid solidification techniques such as water quenching, suction casting, and melt spinning [41,42]. Both Ti and Nb have demonstrated superior catalytic effects in reducing dehydrogenation temperatures and accelerating hydrogen sorption kinetics in MgH<sub>2</sub>.

In this study, a self-synthesized hydride of melt-spun Ti<sub>45</sub>Cr<sub>40</sub>Nb<sub>15</sub> BCC-type hydrogen storage alloy (abbreviated as TiCrNbH<sub>x</sub>-MS) was designed and, for the first time, employed as a catalyst to regulate the hydrogen de-/rehydrogenation performance of MgH<sub>2</sub>. We systematically investigated the catalytic effects of TiCrNbH<sub>x</sub>-MS on the de-/rehydrogenation kinetics, thermodynamics, and cyclic stability of MgH<sub>2</sub>. The microstructure evolution and catalytic mechanisms were also explored, providing valuable insights for the potential commercial application of Mg-based multi-phase composite hydrogen storage materials.

## 2. Experimental section

### 2.1. Sample preparation

The starting materials, including titanium (Ti, sponge, 99.9 %), chromium (Cr, granules, 99.9 %), and niobium (Nb, Aladin, metal powders, 99.99 %), were commercially obtained and used without further purification. The metals Ti and Cr were purchased from Zhongnuo Advanced Material (Beijing) Technology Co., Ltd. The Ti<sub>45</sub>Cr<sub>40</sub>Nb<sub>15</sub> ingots and melt-spun samples (denoted as TiCrNb-AC and TiCrNb-MS, respectively) were synthesized as described in our previous work [39]. Briefly, 10 g ingots of Ti<sub>45</sub>Cr<sub>40</sub>Nb<sub>15</sub> were produced using an arc melting process (WK Series Vacuum Arc Melter, Physcience, China) with a melting current of 100–140 A, and were flipped and remelted four times to ensure compositional homogeneity. The prepared as-cast alloys were

subsequently polished to achieve a clean surface and cut into smaller pieces. Approximately 5 g of these particles were loaded into a quartz tube to prepare ribbons using a single-roller melt-spinning device (VSD500, AutoVac, China) at a roller surface speed of 25 m/s under an argon atmosphere. The resulting melt-spun ribbons (2 g) were loaded into a reactor and sealed for complete hydrogenation using a Sievert-type PCT apparatus (ZDHM-4, Zhejiang University, China) following activation at 400 °C. The final product, melt-spun Ti<sub>45</sub>Cr<sub>40</sub>Nb<sub>15</sub> hydride (labeled as TiCrNbH<sub>x</sub>-MS), was successfully synthesized.

MgH<sub>2</sub> was synthesized via high-temperature hydrogenation followed by mechanical ball milling. Specifically, magnesium powder (Sinopharm Group, 99.95 %) was hydrogenated in a stainless-steel reactor using the aforementioned Sieverts-type apparatus at 400 °C for 6 h under 50 bar of hydrogen pressure. The hydrogenated Mg powder was subsequently transferred to a milling jar under 30 bar of hydrogen and subjected to ball milling at 500 r/m for 5 h, utilizing a ball-to-powder weight ratio of 40:1 in a planetary ball mill (QM-3SP2, Nanjing, China). The process was repeated twice, resulting in the final MgH<sub>2</sub> product. TiCrNbH<sub>x</sub>-MS-modified MgH<sub>2</sub> composites, containing 20 wt% of the hydride, were prepared through mechanical ball milling at 500 r/m under 50 bar of hydrogen for 18 h with a ball-to-sample ratio of 120:1. The milling procedure was set by alternating 12 mins of milling with 6 mins pause to avoid overheating. Every 6 h milling was finished, the jar will be taken back to the glove box for further scraping powder. For comparison, stoichiometrically equivalent Ti (Aladdin, metal powders, 99.99 %) and Nb powders (Aladdin, 99.99 %) were also ball-milled with MgH<sub>2</sub>, with a ball-to-sample ratio of 120:1. All sample handling procedures were conducted in an argon-filled Etelux Lab2000 glove box.

## 2.2. Sample characterization

Phase identification was conducted using X-ray diffraction (XRD, PANalytical X'Pert, Netherlands) with Cu K $\alpha$  radiation (40 kV, 40 mA). To prevent exposure to air and moisture during the XRD analysis, the samples were covered with polyimide film. Morphological and microstructural analyses were performed using field emission scanning electron microscopy (SEM, JEOL JSM-IT800, Japan) and high-resolution transmission electron microscopy (TEM, FEI Talos-F200s, USA). Elemental distributions were characterized using an energy dispersive X-ray spectrometer (EDX, Max) attached to the TEM. Dehydrogenation onset and peak temperatures were measured using differential scanning calorimetry (DSC, Netzsch STA 449F5, Germany) at various heating rates (2, 5, 8, 10 °C·min<sup>-1</sup>) under flowing argon as the purge gas.

## 2.3. Hydrogen storage measurements

For non-isothermal temperature-programmed desorption (TPD) tests, samples were heated from room temperature to 400 °C at a rate of 2 °C·min<sup>-1</sup> using a resistance furnace under vacuum. The dehydrogenated samples were then

recharged at a rate of 1 °C·min<sup>-1</sup> under an initial pressure of 50 bar H<sub>2</sub>. Isothermal de-/rehydrogenation measurements were carried out using the aforementioned Sieverts-type apparatus. Specifically, isothermal hydrogen rehydrogenation was conducted under an initial pressure of 50 bar H<sub>2</sub>, while isothermal hydrogen dehydrogenation was performed under a backpressure of 0.001 bar, with samples rapidly heated to the desired temperature and maintained throughout the entire process.

Pressure-Concentration-Temperature (PCT) measurements were performed using a commercial Sieverts apparatus (HPSA-autoPro device, China), with approximately 150 mg of sample used for each test. Cycling hydrogen de-/rehydrogenation tests were also conducted using this device, with approximately 200 mg of sample subjected to dehydrogenation at a constant temperature of 300 °C under 3 bar H<sub>2</sub> and rehydrogenation under 50 bar H<sub>2</sub> for reversible cycling evaluation.

## 3. Results and discussion

### 3.1. Structure and morphological characterizations

**Fig. 1a** displays the XRD patterns of TiCrNb alloys at various preparation stages. The TiCrNb-AC alloy is characterized by the presence of the primary NbCr<sub>2</sub> (C15 Laves) phase and a Ti-rich body-centered cubic (BCC) phase. After melt spinning, the TiCrNb-MS sample exhibits the typical BCC phase. Upon full rehydrogenation after several activation cycles, the TiCrNbH<sub>x</sub>-MS is entirely converted into a hydride with a face-centered cubic (FCC) phase, which aligns well with previously reported findings [43–45]. **Fig. 1b** presents the SEM image of the TiCrNb-MS alloy, revealing a surface morphology with uniform fine equiaxed crystal grains in the melt-spun alloy. **Fig. 1c** shows that the alloy morphology develops several microcracks on the surface upon full hydrogen recharging. To further examine the microstructure and investigate the alloy's composition, TEM analysis was performed on the fully rehydrogenated TiCrNbH<sub>x</sub>-MS alloy. The elemental mapping obtained from EDX (**Fig. 1d**) indicates that Ti, Cr, and Nb are homogeneously distributed throughout the hydride. **Fig. 1e-f** depict high-resolution TEM (HRTEM) images of the TiCrNbH<sub>x</sub>-MS hydride, showing characteristic lattice spacings of 0.2263 nm and 0.2306 nm, which correspond to the (111) and (111̄) planes of the FCC phase, respectively. The selected area electron diffraction (SAED) pattern (**Fig. 1g**) confirms that the alloy exhibits a typical FCC phase with the [110] zone axis. Additionally, the microcrystalline structure of the TiCrNb-MS alloy was analyzed using TEM to verify the structural evolution during hydrogen de-/rehydrogenation (shown in Fig. S1a-d). Fig. S1a shows continuous diffraction rings corresponding to the (110), (200), and (211) planes of the BCC phase in the TiCrNb-MS alloy. The lattice spacing of 0.2078 nm is attributed to the (110) plane of the BCC phase, as illustrated in Fig. S1c and d. The TEM results corroborate the XRD analysis, confirming the

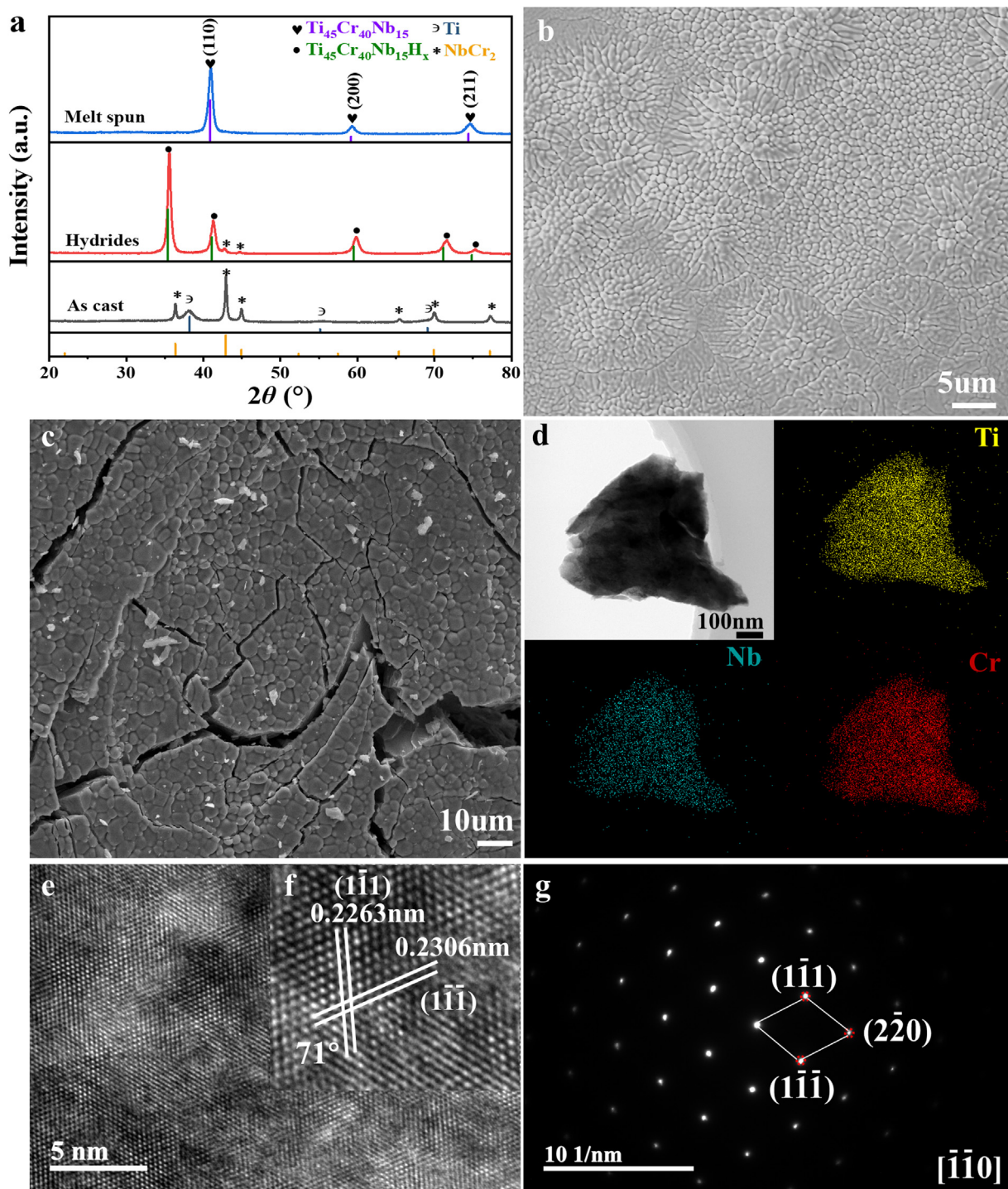


Fig. 1. (a) XRD patterns of the different prepared states of the alloys. (b) SEM image of the TiCrNb-MS alloy. (c) SEM image and (d) STEM and EDX elemental mappings, (e, f) the HRTEM images, (g) SAED pattern of the TiCrNbH<sub>x</sub>-MS alloy.

structural characteristics of both the TiCrNbH<sub>x</sub>-MS hydride and the TiCrNb-MS alloy.

### 3.2. Hydrogen storage performance of TiCrNbH<sub>x</sub>-MS modified MgH<sub>2</sub>

To assess the catalytic effects of the TiCrNbH<sub>x</sub>-MS modified MgH<sub>2</sub> system, non-isothermal and isothermal dehy-

drogenation experiments were conducted on MgH<sub>2</sub> + 20 wt% TiCrNbH<sub>x</sub>-MS, stoichiometric MgH<sub>2</sub>-Ti and MgH<sub>2</sub>-Nb (with equal amounts of Ti and Nb), and ball-milled MgH<sub>2</sub> samples. Fig. 2a displays the TPD volumetric hydrogen release curves of the modified MgH<sub>2</sub> samples, confirming that the catalysts effectively reduce the onset dehydrogenation temperature to varying degrees. The temperature at which the composite releases 0.1 wt% H<sub>2</sub> is denoted as the onset dehydrogenation

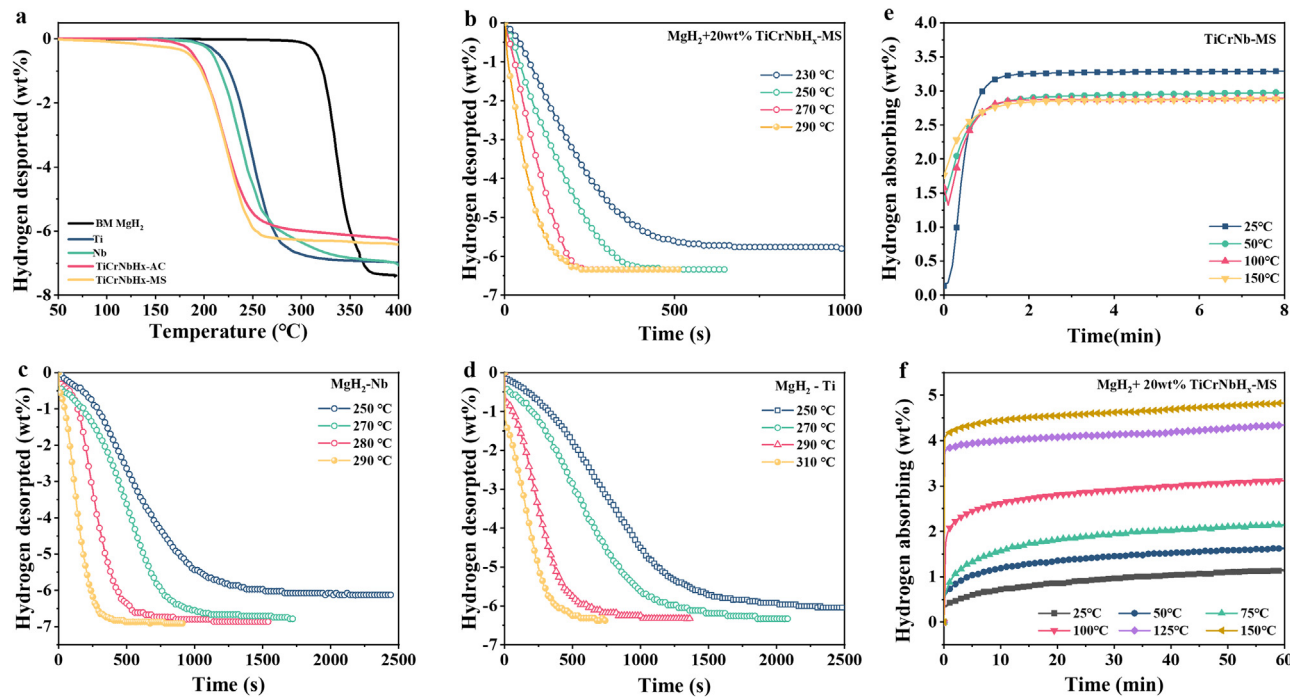


Fig. 2. Temperature-programmed dehydrogenation curves of the MgH<sub>2</sub>/TiCrNbH<sub>x</sub>-MS/AC, and MgH<sub>2</sub>/Ti/Nb composites (a); Isothermal dehydrogenation curves of MgH<sub>2</sub>+20 wt% TiCrNbH<sub>x</sub>-MS (b), MgH<sub>2</sub>-Nb (c) and MgH<sub>2</sub>-Ti (d) at different temperature; Isothermal rehydrogenation curves of TiCrNb-MS (e) and the MgH<sub>2</sub>+20 wt% TiCrNbH<sub>x</sub>-MS composite(f) at different temperature.

temperature [46]. Pristine MgH<sub>2</sub> began releasing hydrogen at approximately 286 °C and fully desorbed ~7.44 wt% H<sub>2</sub>. By adding 20 wt% TiCrNbH<sub>x</sub>-MS to MgH<sub>2</sub>, the onset dehydrogenation temperature was significantly reduced to ~163 °C, with ~6.6 wt% H<sub>2</sub> fully desorbed—representing a reduction of 123 °C compared to pristine MgH<sub>2</sub>. Even with the additive amount increased to 20 wt%, the MgH<sub>2</sub> + TiCrNbH<sub>x</sub>-MS composite retains a high total hydrogen storage capacity, attributed to the intrinsic hydrogen de-/rehydrogenation properties of the melt-spun TiCrNb alloys with a single BCC phase. Furthermore, MgH<sub>2</sub> catalyzed with Ti or Nb showed a similar onset temperature of ~196 °C.

Fig. 2b-d present the isothermal dehydrogenated curves for MgH<sub>2</sub> samples with the respective catalysts. As shown in Fig. 2b, the MgH<sub>2</sub> + 20 wt% TiCrNbH<sub>x</sub>-MS composite desorbed approximately 6.34 wt% hydrogen within 230 s at 270 °C and around 5.80 wt% hydrogen within 700 s at 230 °C. The isothermal dehydrogenation and rehydrogenation curves of pristine MgH<sub>2</sub> at different temperatures are depicted in Fig. S2, showing that nearly no hydrogen release was detected from ball-milled MgH<sub>2</sub> even at 250 °C. Under the same temperature, the dehydrogenation kinetics of the MgH<sub>2</sub> + 20 wt% TiCrNbH<sub>x</sub>-MS composite was significantly better compared to MgH<sub>2</sub> catalyzed by either Ti or Nb alone, as illustrated in Figs. 2c and d. Specifically, MgH<sub>2</sub> catalyzed with stoichiometric amounts of Ti and Nb released approximately 4.53 wt% and 4.80 wt% hydrogen, respectively, within 1000 s at 250 °C. At 200 °C (Fig. S3), MgH<sub>2</sub> catalyzed with Ti and Nb each released 1.0 wt% hydrogen within 3000 s, whereas TiCrNbH<sub>x</sub>-MS-catalyzed MgH<sub>2</sub> desorbed ap-

proximately 2.5 wt% under the same conditions. Clearly, the MgH<sub>2</sub> + TiCrNbH<sub>x</sub>-MS composite exhibited the fastest dehydrogenation rates among the tested samples.

Fig. 2e shows the hydrogen rehydrogenated kinetics curves of the TiCrNb-MS alloy from 25 °C to 150 °C, indicating a maximum hydrogen absorption of 2.83 wt% at 150 °C. Furthermore, with the addition of TiCrNbH<sub>x</sub>-MS, the composite could absorb hydrogen even at room temperature (25 °C). The isothermal rehydrogenation tests of the MgH<sub>2</sub> + 20 wt% TiCrNbH<sub>x</sub>-MS composite at various temperatures (Fig. 2f) reveal that it recharged 1.6 wt% hydrogen within 1 h at 50 °C. The rehydrogenation kinetics improved as the temperature increased, with the composite recharging 2.6 wt% hydrogen in 10 mins and 3.2 wt% in 1 h at 100 °C, and absorbing 4.3 wt% hydrogen within 2 mins at 150 °C. These results indicate that TiCrNbH<sub>x</sub>-MS-catalyzed MgH<sub>2</sub> exhibits excellent rehydrogenation kinetics even at low temperatures.

### 3.3. De-/rehydrogenation kinetics calculation by Chou model

To understand the mechanism behind the enhanced dehydrogenation kinetics, all isothermal dehydrogenation curves were analyzed using the Chou model [47,48]. According to the basically consensus about the hydrogen adsorption process, which can be described as following steps [49]: (a) surface physical/chemical hydrogen adsorption process; (b) surface hydrogen dissociation, penetration and diffusion process of H atoms in  $\beta$ -phase; (c) nucleation and growth process of  $\beta$ -phase; (d) interface chemical reaction process. Actually, the hydrogen diffusion coefficient when passing through the

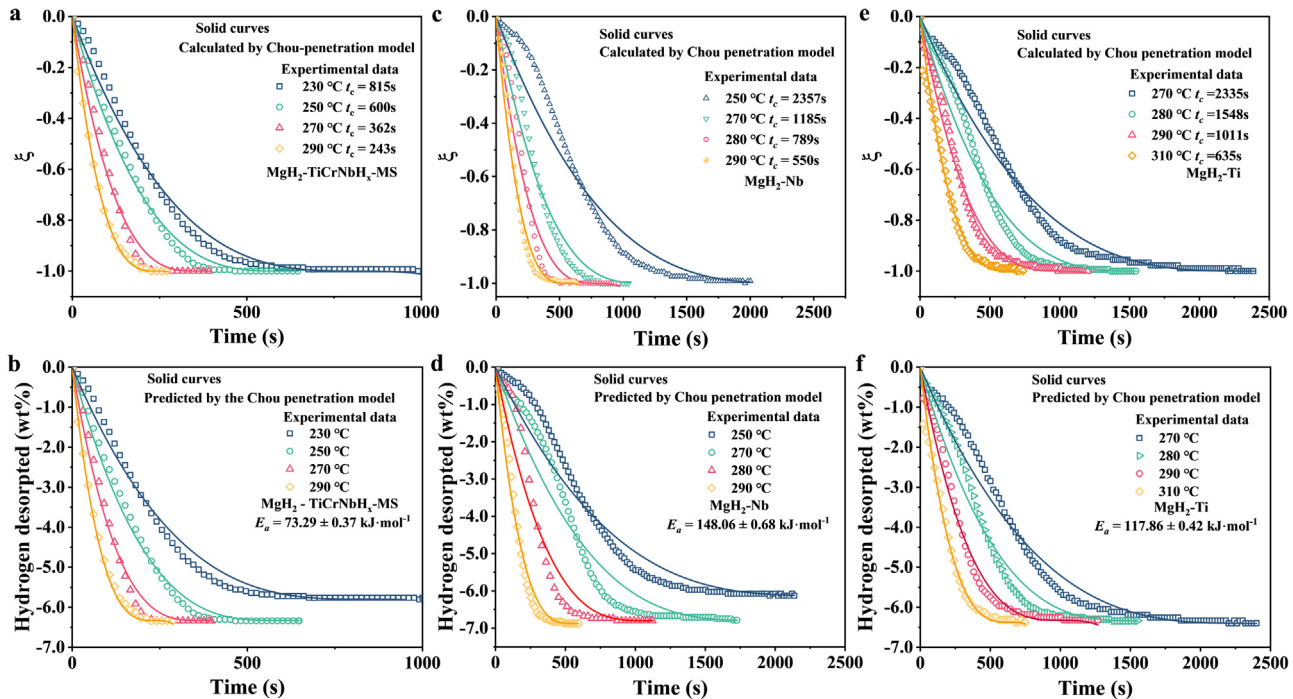


Fig. 3. The reaction fraction and rate control lines at different temperature of  $\text{MgH}_2 + \text{TiCrNbH}_x\text{-MS}$  (a),  $\text{MgH}_2\text{-Nb}$  (b),  $\text{MgH}_2\text{-Ti}$  (c); Experiment data of dehydrogenated and curves obtained by Chou penetration model prediction of  $\text{MgH}_2 + \text{TiCrNbH}_x\text{-MS}$  (d),  $\text{MgH}_2\text{-Nb}$  (e),  $\text{MgH}_2\text{-Ti}$  (f) at different temperature.

passivation layer is very small. Furthermore, the diffusion reaction becomes inactive due to the hydrogen diffusion difference crossing the different phase interfaces. The Chou model provides a physical interpretation of the generalized rate constant and offers a clear expression for calculation and theoretical analysis, which is used to analyze the hydrogen de-/absorption reaction by describing step (b). Specifically, the Chou model describes the functional relationship between the rate and factors such as temperature, pressure, particle size, and equilibrium pressure. It introduces the concept of “characteristic reaction time,  $t_c$ ” and determines the activation energy  $E_a$  to assess the influence of temperature on the rate constant. In summary, when the rate-controlling step is diffusion, the equations can be represented as shown in Eq. (1) [50]:

$$\xi = 1 - \left(1 - \sqrt{\frac{t}{t_c}}\right)^3 \quad (1)$$

when the rate-controlling step is surface penetration, the formulae can be listed as Eq. (2):

$$\xi = 1 - \left(1 - \frac{t}{t_c}\right)^3 \quad (2)$$

where  $\xi$  is the reaction fraction, and  $t$  is the reaction time, respectively. When  $t = t_c$ ,  $\xi = 1$ ,  $t_c$  represents the time required for the complete reaction, referred to as “characteristic reaction time.” A smaller  $t_c$  indicates faster reaction rate. The calculated  $t_c$  values and the predicted dehydrogenation kinetic curves using the Chou model for the respective samples are presented in Table S1 and Figs. 3a-c, respectively. The fitting results indicate that surface penetration is the rate-determining

step for  $\text{MgH}_2$  modified with Ti, Nb, and  $\text{TiCrNbH}_x\text{-MS}$ . The  $t_c$  value of the  $\text{MgH}_2 + 20 \text{ wt\% TiCrNbH}_x\text{-MS}$  composite decreases with increasing temperature, from 815 s at 230 °C to 362 s at 270 °C, which is also the lowest among the three catalyst-modified  $\text{MgH}_2$  samples, even at 270 °C. To evaluate the enhancement in dehydrogenation kinetics achieved by  $\text{TiCrNbH}_x\text{-MS}$  catalysis, the apparent dehydrogenation activation energy Des- $E_a$  can be calculated using Eq. (3) of the Chou penetration model [51]:

$$\xi = 1 - \left[1 - \exp\left(-\frac{E_a}{RT}\right)\frac{t}{B_t}\right]^3 \quad (3)$$

Where  $E_a$  is the activation energy,  $T$  is the temperature,  $R$  is the gas constant, and  $B_t$  is the pressure coefficient. Therefore, the Des- $E_a$  can be calculated as  $73.29 \text{ kJ}\cdot\text{mol}^{-1}$ , and the calculated Des- $E_a$  is much lower than that of the investigated Ti, Nb catalysts and the pristine  $\text{MgH}_2$ , which further clarified the enhanced kinetics catalyzed by the  $\text{TiCrNbH}_x\text{-MS}$ . It is worth noting that the dehydrogenation curves of Ti-, Nb catalyzed  $\text{MgH}_2$  (in Fig. 2c, d) show an anti “S” type, which is considered as a typical feature of the nucleation and growth process [12].

To further verify the dehydrogenation activation energy Des- $E_a$ , DSC measurements were conducted, and the corresponding DSC curves for the catalyst-modified and pristine  $\text{MgH}_2$  at different temperatures, using heating rates of 2, 5, 8, and 10  $^{\circ}\text{C}\cdot\text{min}^{-1}$ , are shown in Figs. 4a-b. Based on the Kissinger Eq. (4):

$$\ln\left(\frac{\beta}{T_m^2}\right) = -\frac{E_a}{RT_m} + A \quad (4)$$

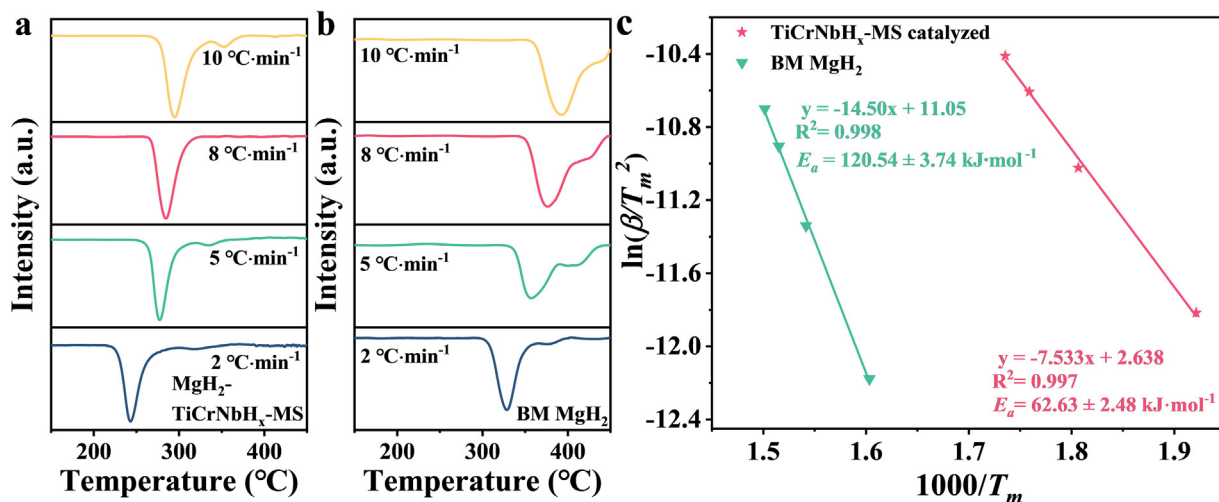


Fig. 4. DSC curves of ball-milled MgH<sub>2</sub>+TiCrNbH<sub>x</sub>-MS(a) and undoped ball milled MgH<sub>2</sub>(b) under the different heating rates (2, 5, 8, 10 °C·min<sup>-1</sup>); The dehydrogenated activation energy fitted by the Kissinger plots of different catalysts doped and undoped MgH<sub>2</sub>(c).

Table 1  
Comparison of properties of different additions catalyzed MgH<sub>2</sub> systems.

Additions catalyzed MgH <sub>2</sub>	Onset dehydrogenated temperature ( °C)	Dehydrogenation activation energy Des-E <sub>a</sub> (kJ·mol <sup>-1</sup> )	Method calculated	Refs.
10 wt%V <sub>80</sub> Ti <sub>12</sub>	208	104.2	Chou model	[49]
20 wt%Ti <sub>0.16</sub> Cr <sub>0.24</sub> V <sub>0.6</sub>	224	131.34	Kissinger equation	[39]
10 wt%Ti	—	104	Kissinger equation	[52]
5 wt%Nb	186.7	90.04	JMAK model	[53]
5 wt%αFe-ZIF	—	104.5	Chou model	[54]
10 wt%TiVNbCrFe	200	63.03	Ozawa-Flynn-Wall	[32]
10 wt%CrMnFeCoNi	198	75.81	Chou model	[55]
5 wt%FeCoNiCrMn	209.1	90.24	JMAK model	[17]
5 wt%NiCoFeCuMg@C	167.3	112.4	Kissinger equation	[29]
20 wt%TiCrNbH <sub>x</sub> -MS	163	73.29	Chou model	This work

Where  $\beta$  is the heating rate,  $T_m$  is the peak temperature, and  $A$  is the temperature-independent constant. By fitting the Kissinger plots derived from the relationship between  $\beta$  and  $T_m$  (shown in Fig. 4c), the dehydrogenated activation energy Des- $E_a$  values were calculated to be 62.63 kJ·mol<sup>-1</sup> for the TiCrNbH<sub>x</sub>-MS-catalyzed MgH<sub>2</sub> composite and 120.54 kJ·mol<sup>-1</sup> for ball-milled pristine MgH<sub>2</sub>. Furthermore, the comparative Nb- and Ti- catalyzed MgH<sub>2</sub> composites were also performed by DSC testing with the same condition. The results are shown in Fig. S4. The Des- $E_a$  values of Nb- and Ti- catalyzed MgH<sub>2</sub> were determined to be 110.82 and 91.66 kJ·mol<sup>-1</sup>, respectively. It represents approximately a 50 % reduction in Des- $E_a$  for TiCrNbH<sub>x</sub>-MS-catalyzed MgH<sub>2</sub> compared to ball-milled MgH<sub>2</sub>. Table 1 presents the initial dehydrogenation temperature and the dehydrogenation activation energy of different additions catalyzed MgH<sub>2</sub> systems. It is found from the table that the TiCrNbH<sub>x</sub>-MS has superior advantages in achieving the lower Des- $E_a$  and the onset dehydrogenation temperature than that of the V-based BCC solid solution catalyzed MgH<sub>2</sub>. Even its catalytic effect is better than the HEAs catalyst prepared by the chemical synthesis.

It is demonstrated that the melt spun TiCrNb indeed has excellent catalytic effect on tuning the comprehensive hydrogen storage performance of MgH<sub>2</sub>.

#### 3.4. Thermodynamic behavior of TiCrNbH<sub>x</sub>-MS modified MgH<sub>2</sub>

To further evaluate the thermodynamic performance of the samples, the dehydrogenation reaction enthalpy changes of the composite and ball-milled MgH<sub>2</sub> were calculated using the van't Hoff equation. Figs. 5a-c show the de/rehydrogenation PCT curves for MgH<sub>2</sub> + TiCrNbH<sub>x</sub>-MS and pristine MgH<sub>2</sub>. The dehydrogenated plateau pressures for MgH<sub>2</sub> + TiCrNbH<sub>x</sub>-MS were determined to be 2.02, 2.91, 5.19, and 8.58 bar at 310, 330, 350, and 370 °C, respectively, while those for ball-milled MgH<sub>2</sub> were measured as 2.42, 4.16, 7.33, and 11.38 bar at 315, 335, 355, and 375 °C, respectively. The corresponding dehydrogenation enthalpy changes ( $ΔH$ ) were also calculated and are shown in Fig. 5c. Notably, the calculated  $ΔH$  value for TiCrNbH<sub>x</sub>-MS-modified MgH<sub>2</sub> was 75.5 kJ·mol<sup>-1</sup> H<sub>2</sub>, which was slightly

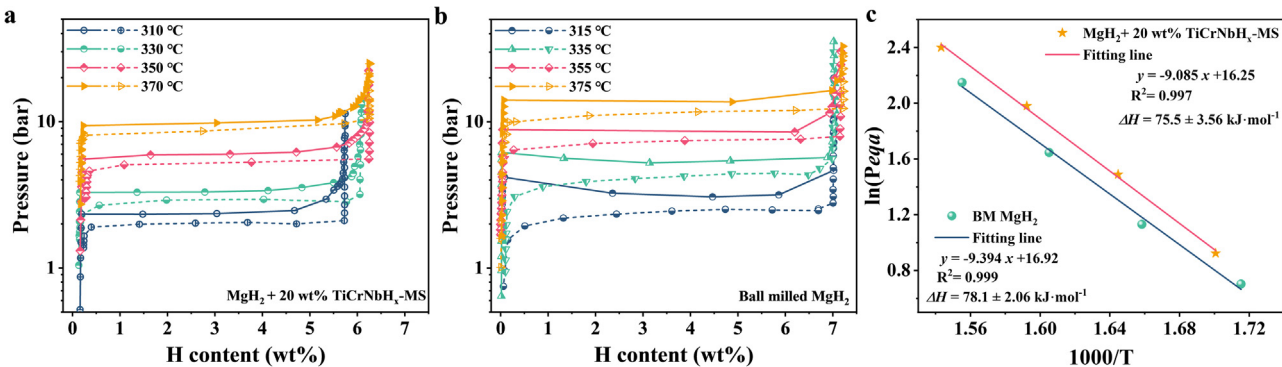


Fig. 5. PCT curves of  $\text{MgH}_2 + \text{TiCrNbH}_x\text{-MS}$ (a); undoped  $\text{MgH}_2$ (b) at different temperature; The Van't Hoff and enthalpies of  $\text{MgH}_2 + \text{TiCrNbH}_x\text{-MS}$  and undoped  $\text{MgH}_2$ (c).

lower than that of pristine  $\text{MgH}_2$  ( $78.1 \text{ kJ}\cdot\text{mol}^{-1} \text{ H}_2$ ). Thus, it indicates that incorporating  $\text{TiCrNbH}_x\text{-MS}$  has minimal effect on the thermodynamic properties of  $\text{MgH}_2$ .

### 3.5. Cycling performance of $\text{TiCrNbH}_x\text{-MS}$ modified $\text{MgH}_2$

Reversible cycling stability is a critical parameter for the practical application of magnesium-based hydrogen storage systems [55,56]. To further evaluate the cycling stability of the  $\text{MgH}_2 + 20 \text{ wt\% TiCrNbH}_x\text{-MS}$  composite, hydrogen de-/rehydrogenation cycling tests were conducted at  $300^\circ\text{C}$ . As shown in Fig. 6a, the reversible hydrogen capacity decreased from 6.18 wt% to 5.03 wt% after 10 cycles. This is often attributed to an “activation process” that occurs during the initial de-/rehydrogenation cycles, as reported in previous studies [19,57,58]. The detailed data profiles (Fig. S5) for the 1st, 30 th, 50 th, and 100 th cycle indicate that it took about 5 mins for the composite to release its full hydrogen content during the first dehydrogenation, while subsequent cycles only took approximately 3 mins. The composite exhibited a rapid hydrogen uptake and release rate over 100 cycles, with a capacity degradation from 6.18 wt% to 4.98 wt%. This corresponds to a hydrogen capacity retention of 81 %, as shown in Fig. 6c. The results demonstrate that the rapid decline in hydrogen capacity occurred during the initial few cycles in the  $\text{MgH}_2 + 20 \text{ wt\% TiCrNbH}_x\text{-MS}$  system, after which the dehydrogenation capacity remained stable in the following cycles. The XRD patterns results (shown in Fig. S6) reveal that there is no new phase generated after cycling. In order to further explore the effect of cycling on kinetic performance, the de-/rehydrogenation data were computationally analyzed by kinetic model. According to the previous analysis, it implies that the rate-controlling step of hydrogen de-/rehydrogenation process of the  $\text{MgH}_2 + 20 \text{ wt\% TiCrNbH}_x\text{-MS}$  composite was the surface penetration. Actually, Mg can instantaneously nucleate on the particle surface and it is feasible for metal atoms to achieve the long-range diffusion and the diffusion of H atoms into the hydride layer under high temperature. The nucleation and growth of Mg and H diffusion during dehydrogenation can be rapidly finished. The  $t_c$  values calculated by the Chou-penetration model were analyzed to evaluate the variation of the dehydrogenated kinetic property during the cycle, as presented in Fig. 6b. The  $t_c$  values rapidly decrease at the beginning and then slightly increase with cycling numbers ascending. The kinetic performance from 40 to 100 cycles is relatively stable. As reported, the phase transition between Mg-MgH<sub>2</sub> will occur 32 % volume expansion or contraction [12]. However, the powder agglomeration will inevitably exist under long-term high temperature. This phenomenon will make hydrogen penetration more difficult during few initial cycles. After that, particle cracking happens and smaller particles and larger specific surface area can be achieved. It is beneficial to hydrogen penetration ascribed that there are more active sites and providing more penetration driving energy.

Reversible cycling stability is a critical parameter for the practical application of magnesium-based hydrogen storage systems [55,56]. To further evaluate the cycling stability of the  $\text{MgH}_2 + 20 \text{ wt\% TiCrNbH}_x\text{-MS}$  composite, hydrogen de-/rehydrogenation cycling tests were conducted at  $300^\circ\text{C}$ . As shown in Fig. 6a, the reversible hydrogen capacity decreased from 6.18 wt% to 5.03 wt% after 10 cycles. This is often attributed to an “activation process” that occurs during the initial de-/rehydrogenation cycles, as reported in previous studies [19,57,58]. The detailed data profiles (Fig. S5) for the 1st, 30 th, 50 th, and 100 th cycle indicate that it took about 5 mins for the composite to release its full hydrogen content during the first dehydrogenation, while subsequent cycles only took approximately 3 mins. The composite exhibited a rapid hydrogen uptake and release rate over 100 cycles, with a capacity degradation from 6.18 wt% to 4.98 wt%. This corresponds to a hydrogen capacity retention of 81 %, as shown in Fig. 6c. The results demonstrate that the rapid decline in hydrogen capacity occurred during the initial few cycles in the  $\text{MgH}_2 + 20 \text{ wt\% TiCrNbH}_x\text{-MS}$  system, after which the dehydrogenation capacity remained stable in the following cycles. The XRD patterns results (shown in Fig. S6) reveal that there is no new phase generated after cycling. In order to further explore the effect of cycling on kinetic performance, the de-/rehydrogenation data were computationally analyzed by kinetic model. According to the previous analysis, it implies that the rate-controlling step of hydrogen de-/rehydrogenation process of the  $\text{MgH}_2 + 20 \text{ wt\% TiCrNbH}_x\text{-MS}$  composite was the surface penetration. Actually, Mg can instantaneously nucleate on the particle surface and it is feasible for metal atoms to achieve the long-range diffusion and the diffusion of H atoms into the hydride layer under high temperature. The nucleation and growth of Mg and H diffusion during dehydrogenation can be rapidly finished. The  $t_c$  values calculated by the Chou-penetration model were analyzed to evaluate the variation of the dehydrogenated kinetic property during the cycle, as presented in Fig. 6b. The  $t_c$  values rapidly decrease at the beginning and then slightly increase with cycling numbers ascending. The kinetic performance from 40 to 100 cycles is relatively stable. As reported, the phase transition between Mg-MgH<sub>2</sub> will occur 32 % volume expansion or contraction [12]. However, the powder agglomeration will inevitably exist under long-term high temperature. This phenomenon will make hydrogen penetration more difficult during few initial cycles. After that, particle cracking happens and smaller particles and larger specific surface area can be achieved. It is beneficial to hydrogen penetration ascribed that there are more active sites and providing more penetration driving energy.

### 3.6. Microstructure evolution and mechanism analysis of $\text{TiCrNbH}_x\text{-MS}$ modified $\text{MgH}_2$

The  $\text{TiCrNbH}_x\text{-MS}$  catalyst exhibited a remarkable catalytic effect on the hydrogen storage behavior of  $\text{MgH}_2$ , as demonstrated in the above analysis. To further understand the role of  $\text{TiCrNbH}_x\text{-MS}$  in enhancing the hydrogen storage properties of  $\text{MgH}_2$ , the microstructural evolution of ball-milled  $\text{TiCrNbH}_x\text{-MS}$ -modified  $\text{MgH}_2$  during the de-/rehydrogenation process was investigated using X-ray diffraction (XRD). Fig. 7a shows the XRD patterns of the ball-milled, rehydrogenated, and dehydrogenated states of the  $\text{TiCrNbH}_x\text{-MS}$ -modified  $\text{MgH}_2$  composite. From the XRD patterns of the ball-milled state, the main diffraction peaks are identified as belonging to the  $\text{MgH}_2$  phase (P42/mnm, JCPDS: 12-0697). Additionally, a diffraction peak at  $41.6^\circ$  corresponds to the  $\text{TiCrNbH}_x\text{-MS}$  hydride, while peaks at  $43.1^\circ$  and  $45.2^\circ$  correspond to the  $\text{NbCr}_2$  phase. This indicates that no reaction occurred between  $\text{MgH}_2$  and the catalyst, as no new phases were detected after ball milling.

When the composite was ball-milled under 50 bar hydrogen pressure, the  $\text{TiCrNbH}_x\text{-MS}$  hydride was clearly detected. In the XRD pattern of the dehydrogenated state, the predominant phase was  $\alpha\text{-Mg}$  (P63/mmc, JCPDS: 65-3365), along with some diffraction peaks belonging to the BCC and FCC phases of the melt-spun  $\text{TiCrNb}$  alloy [59]. After full

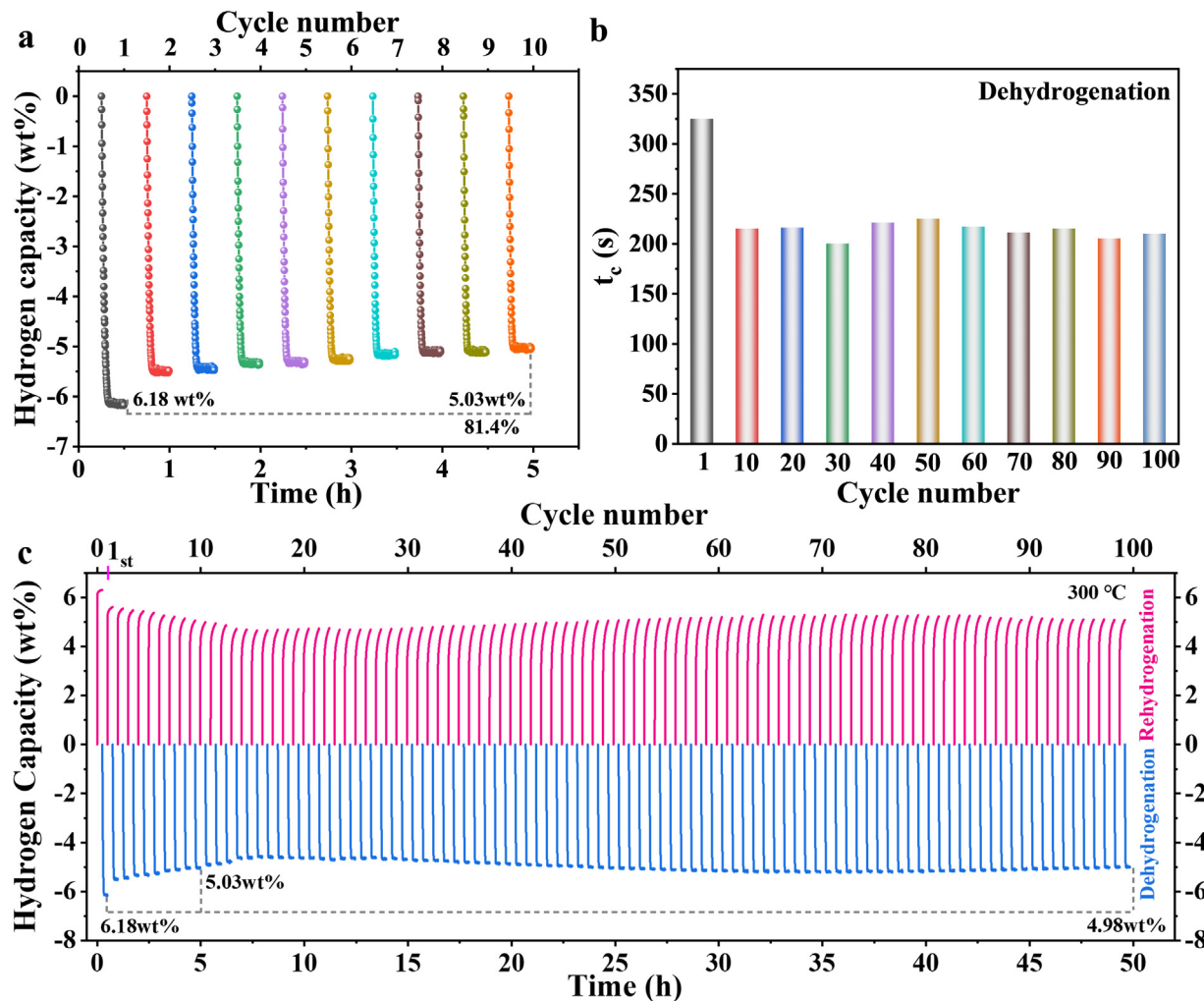


Fig. 6. The dehydrogenation performance of the  $\text{MgH}_2+\text{TiCrNbH}_x\text{-MS}$  composite for the first 10 cycles at 300 °C (a); The characteristic time ( $t_c$ ) with cycling numbers corresponding to the dehydrogenated kinetics of the  $\text{MgH}_2+\text{TiCrNbH}_x\text{-MS}$  sample(b); 100 cycling rehydrogenation and dehydrogenation curves of the  $\text{MgH}_2+\text{TiCrNbH}_x\text{-MS}$  sample (c).

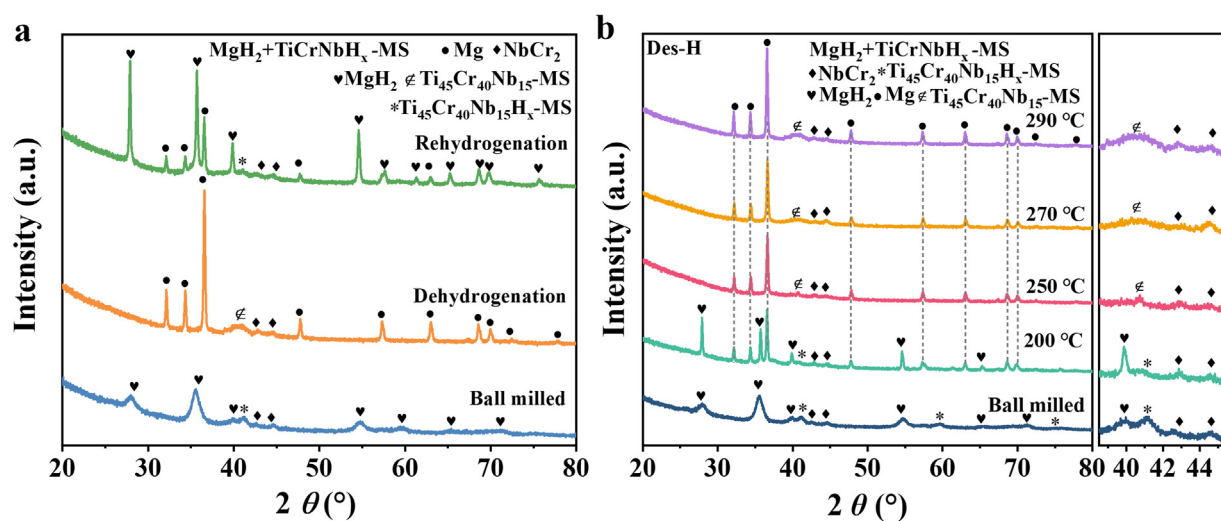


Fig. 7. XRD patterns of the  $\text{MgH}_2+\text{TiCrNbH}_x\text{-MS}$  composite in the ball milled; and de/rehydrogenated states(a); XRD patterns of the  $\text{MgH}_2+\text{TiCrNbH}_x\text{-MS}$  composite under the different dehydrogenated temperature(b).

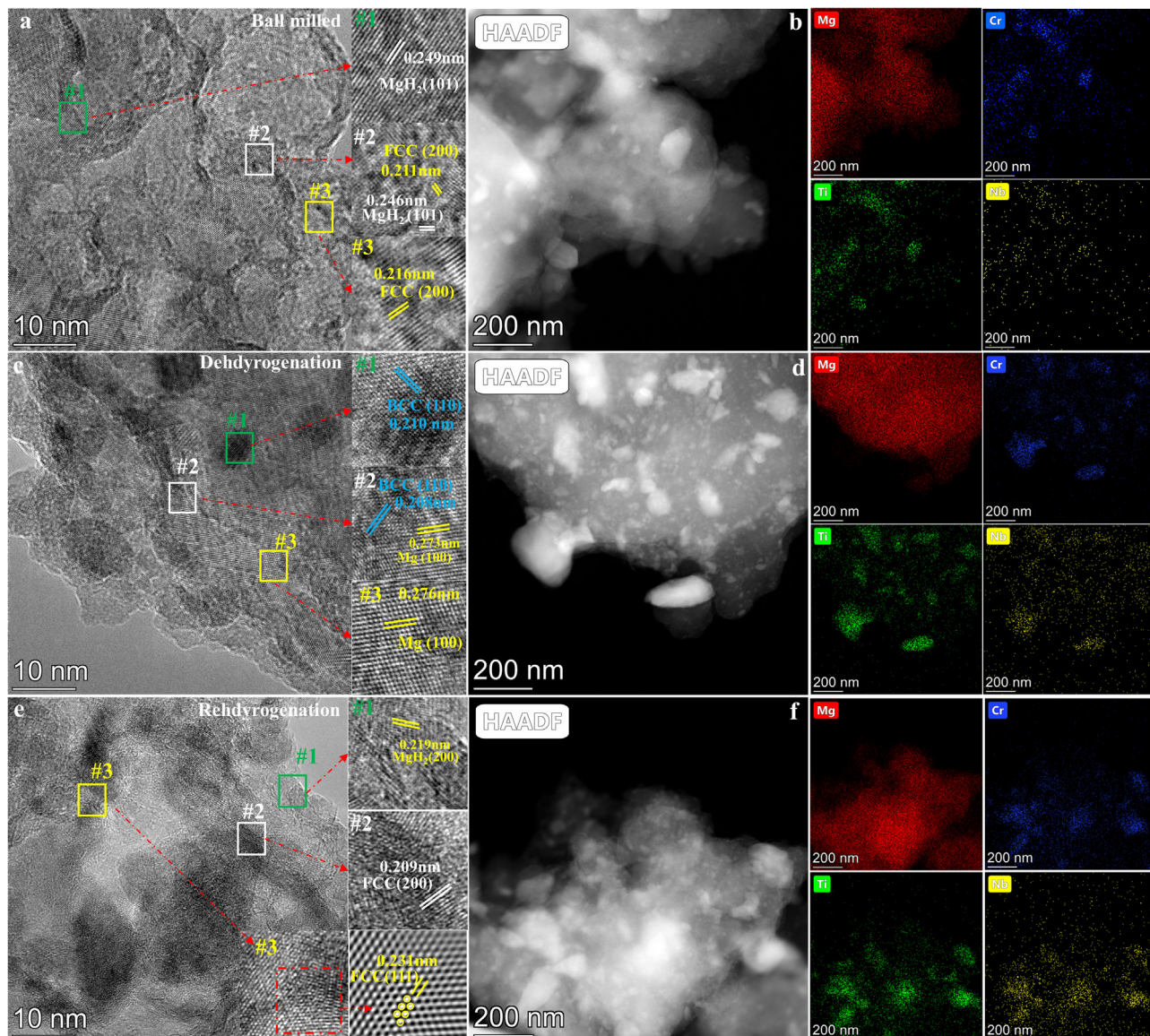


Fig. 8. HRTEM images (a, c, e), HAADF images and corresponding EDS mappings (b, d, f) of the ball milled, dehydrogenated and rehydrogenated state of the  $\text{MgH}_2+\text{TiCrNbH}_x\text{-MS}$  composite.

rehydrogenation, the composite consisted mainly of  $\text{MgH}_2$ , the FCC phase of the melt-spun  $\text{TiCrNb}$  alloy, and a minor  $\text{Mg}$  phase. Furthermore, Fig. 7b shows the XRD patterns of the composite under different dehydrogenation temperatures. The XRD results indicate that the  $\text{MgH}_2$  phase was detected after dehydrogenation at 200 °C and disappeared when the process was carried out at 250 °C. At higher temperatures, the hydrogenated  $\text{TiCrNbH}_x\text{-MS}$  transformed into the BCC structure of the  $\text{TiCrNb-MS}$  alloy during ball milling with  $\text{MgH}_2$  in the dehydrogenation process.

To further reveal the microstructural features of this system, TEM analysis was conducted on  $\text{MgH}_2 + \text{TiCrNbH}_x\text{-MS}$  in different states. As shown in Fig. 8a, the measured interplanar spacing  $d$  value of 0.249 nm corresponds to the (101) lattice plane of the  $\text{MgH}_2$  phase in the ball-milled state. The measured  $d$  values of 0.216 nm and 0.211 nm match the (200)

plane of the FCC phase of the  $\text{TiCrNbH}_x\text{-MS}$  alloy. Additionally, elemental mapping results (Fig. 8b) show that Ti, Cr, and Nb from the  $\text{TiCrNb}$  nanoparticles are uniformly distributed in the  $\text{MgH}_2$  matrix. After dehydrogenation, the characteristic spacing values of 0.273 nm and 0.276 nm were assigned to the (100) lattice plane of the  $\alpha\text{-Mg}$  phase (P63/mmc, JCPDS: 65-3365), as depicted in Fig. 8c. The measured spacing values of 0.210 nm and 0.208 nm were attributed to the (110) lattice plane of the BCC phase of the  $\text{TiCrNb-MS}$  alloy. It is evident that the dehydrogenated composite consists of nano-sized dark-gray  $\text{TiCrNb}$  phase spots embedded in the  $\text{MgH}_2$  matrix. The HRTEM image of the sample after rehydrogenation is presented in Fig. 8e, showing a spacing of 0.219 nm and 0.231 nm, corresponding to the (200) lattice plane of the  $\text{MgH}_2$  phase and the (200) lattice plane of the FCC phase of the  $\text{TiCrNbH}_x\text{-MS}$  alloy, respectively. As depicted in

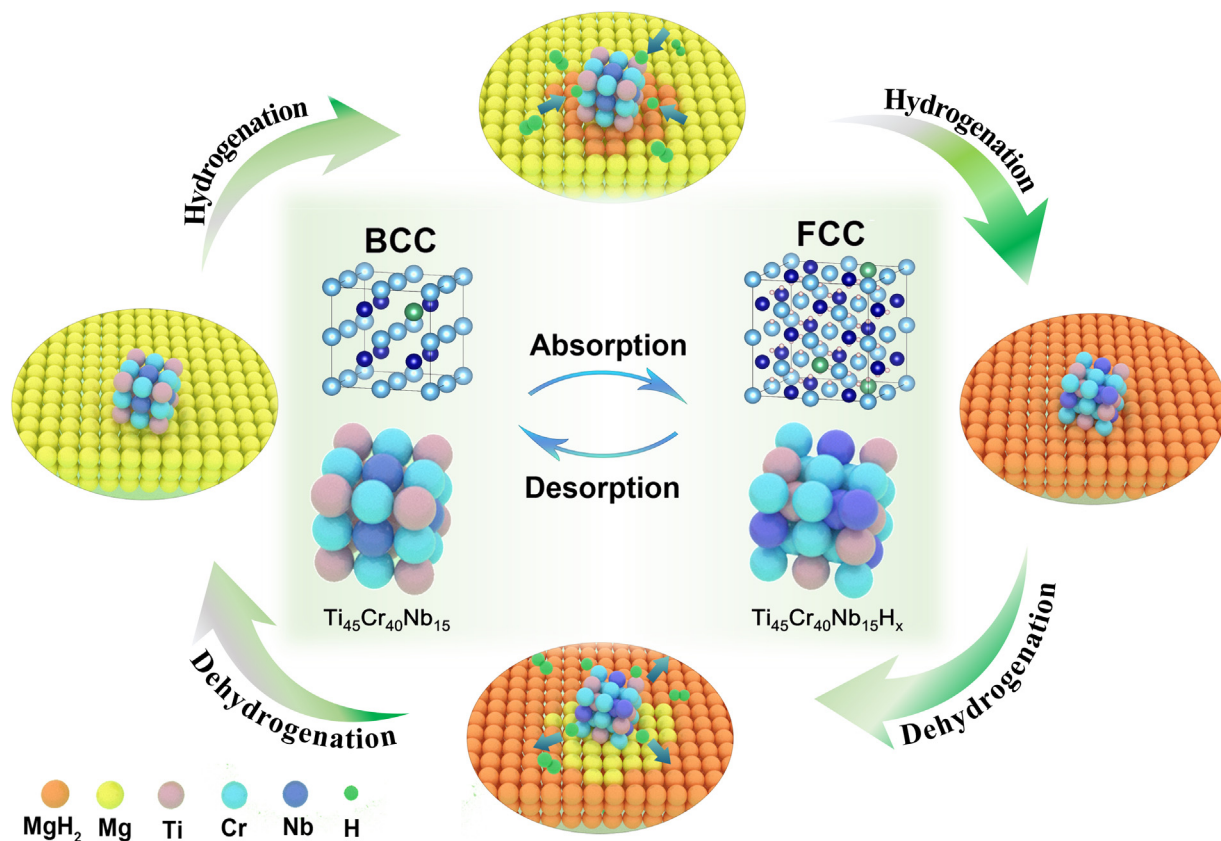


Fig. 9. Schematic summary of catalytic mechanism of the  $\text{TiCrNbH}_x$ -MS modified  $\text{MgH}_2$ .

**Fig. 8f**, the distribution of the elements Ti, Cr, and Nb indicates that the nanosized TiCrNb phase is uniformly embedded in the  $\text{MgH}_2$  matrix.

Based on the aforementioned hydrogen storage properties and microstructural analysis, the de-/rehydrogenation mechanism of the  $\text{MgH}_2 + \text{TiCrNbH}_x$ -MS composite is illustrated in Fig. 9. The uniformly dispersed  $\text{TiCrNbH}_x$ -MS particles act as “hydrogen pumps,” accelerating hydrogen absorption and dissociation due to their superior kinetics. Certainly, the electronegativity of Ti (1.54) or Nb (1.6), being between that of H (2.2) and Mg (1.31), which has been verified to indeed weaken the Mg-H bond energy [60–62]. Additionally, the melt-spun  $\text{TiCrNbH}_x$ -MS alloy contains significant lattice distortion and defects, further facilitating hydrogen diffusion into the Mg lattice via the interfaces. During dehydrogenation, Mg-H bonds at the  $\text{MgH}_2/\text{TiCrNb}$  interfaces are preferentially weakened due to additional interface energy, which subsequently induces lattice distortion in Mg, promoting hydrogen release.

Moreover, the fully hydrogenated TiCrNb alloy with the FCC phase transforms into the BCC phase when the composite undergoes dehydrogenation at elevated temperatures. This phase transformation provides numerous hydrogen diffusion channels and active nucleation sites for Mg/ $\text{MgH}_2$ . During rehydrogenation, hydrogen first diffuses into the TiCrNb alloy and then migrates into the Mg matrix along the Mg/TiCrNb interfaces, ultimately forming the  $\text{MgH}_2$  phase. The BCC phase then reversibly transforms back to the FCC phase

of the TiCrNb alloy upon rehydrogenation. Therefore, the  $\text{TiCrNbH}_x$ -MS alloy actively catalyzes hydrogen combination and dissociation, enhancing the overall de-/rehydrogenation performance of  $\text{MgH}_2$ .

#### 4. Conclusion

In this study, the  $\text{Ti}_{45}\text{Cr}_{40}\text{Nb}_{15}$  alloy was synthesized via melt spinning and then fully hydrogenated. The catalytic effect of adding 20 wt%  $\text{Ti}_{45}\text{Cr}_{40}\text{Nb}_{15}\text{H}_x$ -MS to  $\text{MgH}_2$  through ball milling was investigated to enhance the hydrogen storage performance of  $\text{MgH}_2$ . The  $\text{TiCrNbH}_x$ -MS-catalyzed  $\text{MgH}_2$  composite exhibited an impressive initial dehydrogenation temperature of 163 °C, and the dehydrogenated state was able to readily absorb hydrogen at room temperature. According to the Chou model, the rate-controlling step of dehydrogenation was determined to be surface penetration, and the dehydrogenation activation energy  $E_a$  was reduced to 73.29 kJ·mol<sup>-1</sup>. Furthermore, the composite demonstrated a reversible hydrogen capacity retention of 81 % over 100 cycles at 300 °C.

Microstructural analyses using XRD and TEM revealed that the FCC phase of the melt-spun  $\text{TiCrNbH}_x$ -MS hydride, when ball-milled, reversibly transformed into the BCC phase during the de-/rehydrogenation process. This phase transformation generated additional interfaces dispersed on the  $\text{MgH}_2$  surface, providing more hydrogen diffusion channels and nucleation sites for Mg/ $\text{MgH}_2$ , thereby enhancing the hydrogen de-/rehydrogenation kinetics of the system. This work serves

as a reference for using multiphase composite modification methods to improve the hydrogen storage characteristics of MgH<sub>2</sub>.

### Declaration of competing interest

The authors declare that they have no known competing financial interests or personal relationships that could have appeared to influence the work reported in this paper.

### CRediT authorship contribution statement

**Houqun Xiao:** Writing – original draft, Methodology, Investigation, Formal analysis, Data curation, Conceptualization. **Luocai Yi:** Writing – review & editing, Investigation, Formal analysis, Conceptualization. **Huxu Lei:** Software, Formal analysis, Data curation. **Yu Xu:** Visualization, Methodology, Formal analysis, Conceptualization. **Xiaoxuan Zhang:** Software, Methodology, Investigation, Data curation. **Huazhou Hu:** Resources, Project administration, Investigation, Formal analysis. **Rui Zhu Tang:** Validation, Resources, Formal analysis, Conceptualization. **Qian Li:** Writing – review & editing, Supervision, Resources, Funding acquisition. **Qingjun Chen:** Writing – review & editing, Supervision, Resources, Investigation, Funding acquisition.

### Acknowledgments

This work was financially supported by the National Key Research and Development program of China (2022YFB3504700), the National Natural Science Foundation of China (U23A20128), the Strategic Priority Research Program of the Chinese Academy of Sciences (XDA0400304) and the Research Projects of Ganjiang Innovation Academy, Chinese Academy of Sciences (No. E355B0020).

### Supplementary materials

Supplementary material associated with this article can be found, in the online version, at doi:10.1016/j.jma.2025.01.005.

### References

- [1] M.D. Allendorf, V. Stavila, J.L. Snider, M. Witman, M.E. Bowden, K. Brooks, B.L. Tran, T. Autrey, Nat Chem 14 (2022) 1214–1223.
- [2] T. He, P. Pachfule, H. Wu, Q. Xu, P. Chen, Nat Rev Mater 1 (2016) 16059.
- [3] M.R. Usman, Renew Sustainable Energy Rev 167 (2022) 112743.
- [4] H.T. Guan, Y.J. Liu, X.M. Hu, J.Z. Wu, T.N. Ye, Y.F. Lu, H. Hosono, Q. Li, F.S. Pan, Angewandte Chemie-Int Edition 63 (2024) e202400119.
- [5] G.Kubilay Karayel, N. Javani, I. Dincer, Energy Convers Manag 291 (2023) 117311.
- [6] Z.Y. Li, S.Y. Liu, Y.H. Pu, G. Huang, Y.B. Yuan, R.Q. Zhu, X.F. Li, C.Y. Chen, G. Deng, H.H. Zou, P. Yi, M. Fang, X. Sun, J.Z. He, H. Cai, J.X. Shang, X.F. Liu, R.H. Yu, J.L. Shui, Nat. Commun. 14 (2023) 7966.
- [7] S. Niaz, T. Manzoor, A.H. Pandith, Renew Sustainable Energy Rev 50 (2015) 457–469.
- [8] T. Ha, J.-H. Kim, C. Sun, Y.-S. Lee, D.-I. Kim, J.-Y. Suh, J.-I. Jang, J. Lee, Y. Kim, J.-H. Shim, Nano Energy 112 (2023) 108483.
- [9] W.F. Qiao, D.M. Yin, S.L. Zhao, N. Ding, L. Liang, C.L. Wang, L.M. Wang, M. He, Y. Cheng, Chem. Eng. J. 465 (2023) 142837.
- [10] S. Thiangviriya, P. Thongtan, N. Thaweeplap, P. Plerdsranoy, R. Utke, Int. J. Hydrogen Energy 49 (2024) 59–66.
- [11] Q. Li, Y.F. Lu, Q. Luo, X.H. Yang, Y. Yang, J. Tan, Z.H. Dong, J. Dang, J.B. Li, Y. Chen, B. Jiang, S.H. Sun, F.S. Pan, J Magnesium Alloys 9 (2021) 1922–1941.
- [12] B. Li, X. Sun, H. Chen, Y. Yang, Q. Luo, X.H. Yang, Y.A. Chen, G.B. Wei, Q. Li, F.S. Pan, J Mater Sci Technol 180 (2024) 45–54.
- [13] Q. Luo, Q. Cai, Q.F. Gu, Y. Shi, B. Liu, X.Q. Tran, S. Matsumura, T.Y. Zhang, K. Nogita, T. Lyu, Q. Li, F.S. Pan, J Magnes Alloys 11 (2023) 3338–3349.
- [14] H.Y. Wang, J. Li, X.L. Wei, Y. Zheng, S.L. Yang, Y.F. Lu, Z. Ding, Q. Luo, Q. Li, F.S. Pan, Adv Funct Mater (2024) 2406639.
- [15] Z. Ding, Y.T. Li, H. Yang, Y.F. Lu, J. Tan, J.B. Li, Q. Li, Y.A. Chen, L.L. Shaw, F.S. Pan, J Magnesium and Alloys 10 (2022) 2946–2967.
- [16] X.F. Tan, M.J. Kim, K. Yasuda, K. Nogita, J Materials Sci Technol 153 (2023) 139–158.
- [17] H.Y. Wan, X. Yang, S.M. Zhou, L. Ran, Y.F. Lu, Y.A. Chen, J.F. Wang, F.S. Pan, J Mater Sci Technol 149 (2023) 88–98.
- [18] Y.X. Yang, X. Zhang, L.C. Zhang, W.X. Zhang, H.F. Liu, Z.G. Huang, L.M. Yang, C.D. Gu, W.P. Sun, M.X. Gao, Y.F. Liu, H.G. Pan, J Mater Sci Technol 163 (2023) 182–211.
- [19] S.Y. Shen, W.F. Liao, Z.J. Cao, J.W. Liu, H. Wang, L.Z. Ouyang, J Mater Sci Technol 178 (2024) 90–99.
- [20] H.Y. Shao, J. Matsuda, H.W. Li, E. Akiba, A. Jain, T. Ichikawa, Y. Kojima, Int. J. Hydrogen Energy 38 (2013) 7070–7076.
- [21] G. Han, Y.F. Lu, H.X. Jia, Z. Ding, L. Wu, Y. Shi, G.Y. Wang, Q. Luo, Y.A. Chen, J.F. Wang, G.S. Huang, X.Y. Zhou, Q. Li, F.S. Pan, J Magnesium and Alloys 11 (2023) 3896–3925.
- [22] B. Zhang, X.B. Xie, Y.K. Wang, C.X. Hou, X.Q. Sun, Y.P. Zhang, X.Y. Yang, R.H. Yu, W. Du, J Magnesium and Alloys 12 (2024) 1356–1370.
- [23] K. Zhang, Y. Chang, J.J. Lei, J. Chen, T.Z. Si, X.L. Ding, P. Cui, H.W. Li, Q.A. Zhang, Y.T. Li, J Magnesium and Alloys 12 (2024) 2462–2471.
- [24] L.C. Zhang, X. Zhang, W.X. Zhang, Z.G. Huang, F. Fang, J. Li, L.M. Yang, C.D. Gu, W.P. Sun, M.X. Gao, H.G. Pan, Y.F. Liu, ACS Appl. Mater. Interfaces 15 (2023) 40558–40568.
- [25] J. Cui, J.W. Liu, H. Wang, L.Z. Ouyang, D.L. Sun, M. Zhu, X.D. Yao, J Mater Chemistry A 2 (2014) 9645–9655.
- [26] L.T. Zhang, X.Z. Xiao, C.C. Xu, J.G. Zheng, X.L. Fan, J. Shao, S.Q. Li, H.W. Ge, Q.D. Wang, L.X. Chen, J. Phys. Chem. C 119 (2015) 8554–8562.
- [27] M. Jangir, A. Jain, S. Agarwal, T.F. Zhang, S. Kumar, S. Selvaraj, T. Ichikawa, I.P. Jain, Int J Energy Res 42 (2018) 1139–1147.
- [28] L. Dan, H. Wang, X.B. Yang, J.W. Liu, L.Z. Ouyang, M. Zhu, ACS Appl. Mater. Interfaces 15 (2023) 30372–30382.
- [29] Y.F. Liu, M.Y. Yue, Y.S. Guo, Y.R. Jiang, Y. Sun, L.Z. Feng, Y.J. Wang, J Magnesium and Alloys (2024) available online.
- [30] M.X. Wei, Y.J. Liu, X.F. Xing, Z. Zhang, T. Liu, Chem. Eng. J. 476 (2023) 146639.
- [31] J.X. Zhang, H. Liu, C.S. Zhou, P. Sun, X.Y. Guo, Z. Z. Fang, J Mater Chemistry A 11 (2023) 4789–4800.
- [32] K. Kitabayashi, K. Edalati, H.W. Li, E. Akiba, Z. Horita, Adv Eng Mater 22 (2020) 1900027.
- [33] C.S. Zhou, Z.G.Z. Fang, C. Ren, J.Z. Li, J. Lu, J. Phys. Chem. C 117 (2013) 12973–12980.
- [34] Z.F. Li, Y.F. Lu, J.F. Wang, Y.A. Chen, Q. Li, F.S. Pan, Mater Rep (2023) 100247.
- [35] Z.Q. Lu, H.Z. Liu, H. Luo, Z.Y. Wu, H. Ning, Y. Fan, X.H. Wang, X.T. Huang, C.K. Huang, Z.Q. Lan, W.Z. Zhou, J. Guo, Chem. Eng. J. 479 (2024) 147893.
- [36] X. Lu, L.T. Zhang, H.J. Yu, Z.Y. Lu, J.H. He, J.G. Zheng, F.Y. Wu, L.X. Chen, Chem. Eng. J. 422 (2021) 130101.
- [37] G. Liang, J. Huot, S. Boily, A. Van Neste, R. Schulz, J Alloys Compd 297 (2000) 261–265.

- [38] X.B. Yu, Y.H. Guo, H. Yang, Z. Wu, D.M. Grant, G.S. Walker, *J. Phys. Chem. C* 113 (2009) 5324–5328.
- [39] J.F. Zhang, Z.N. Li, Y.F. Wu, X.M. Guo, J.H. Ye, B.L. Yuan, H.P. Yuan, S.M. Wang, L.J. Jiang, *J. Phys. Chem. C* 123 (2019) 15963–15976.
- [40] K. Kubo, H. Itoh, T. Takahashi, T. Ebisawa, T. Kabutomori, Y. Nakamura, E. Akiba, *J. Alloys Compd* 356–357 (2003) 452–455.
- [41] H.Q. Xiao, H.Z. Hu, J. Li, C.M. Ma, Q.J. Chen, *Int. J. Hydrogen Energy* 48 (2023) 22174–22182.
- [42] H.Z. Hu, H.Q. Xiao, J. Li, C.M. Ma, L.C. Yi, Q.J. Chen, *Chem. Eng. J.* 455 (2023) 140970.
- [43] M. Wang, Y. Wang, H. Kong, Q. Xie, C. Wu, Y. Wang, Y. Chen, Y. Yan, *J. Alloys Compd* 958 (2023) 170294.
- [44] E. Halpren, X. Yao, Z.W. Chen, C.V. Singh, *Acta Mater* 270 (2024) 119841.
- [45] T. Tamura, T. Kazumi, A. Kamegawa, H. Takamura, M. Okada, *J. Alloys Compd* 356–357 (2003) 505–509.
- [46] N. Ding, W.Q. Liu, B.B. Chen, S.H. Wang, S.L. Zhao, Q.S. Wang, C.L. Wang, D.M. Yin, L.M. Wang, Y. Cheng, *Chem. Eng. J.* 470 (2023) 144143.
- [47] Y.P. Pang, Q. Li, *Int. J. Hydrogen Energy* 41 (2016) 18072–18087.
- [48] S. Guemou, L.T. Zhang, S. Li, Y.Q. Jiang, T. Zhong, Z.C. Lu, R. Zhou, F.Y. Wu, Q. Li, *J. Mater Sci Technol* 172 (2024) 83–93.
- [49] L.Z. Shen, Z.F. Li, Y.F. Lu, G.B. Wei, Q. Li, Y. Yang, F.S. Pan, *J. Alloys Compd* 1010 (2025) 177591.
- [50] X. Sun, X.H. Yang, Y.F. Lu, Q. Luo, C.Z. Wu, Y. Zhang, T. Lyu, Q.F. Gu, Q. Li, F.S. Pan, *J. Mater Sci Technol* 202 (2024) 119–128.
- [51] H.M. Yang, X. Sun, Q. Luo, Y.F. Lu, Q. Li, F.S. Pan, *Scr. Mater.* 239 (2024) 115782.
- [52] Y.J. Choi, J.W. Choi, H.Y. Sohn, T. Ryu, K.S. Hwang, Z.Z. Fang, *Int. J. Hydrogen Energy* 34 (2009) 7700–7706.
- [53] F.M. Nyahuma, L.T. Zhang, M.C. Song, X. Lu, B.B. Xiao, J.G. Zheng, F.Y. Wu, *Int. J. Minerals, Metall. Mater.* 29 (2022) 1788–1797.
- [54] S.K. Verma, S.S. Mishra, N.K. Mukhopadhyay, T.P. Yadav, *Int. J. Hydrogen Energy* 50 (2024) 749–762.
- [55] J.Y. Lin, W.W. Luo, Z.W. Wu, H.Y. Leng, C.H. Sun, Q. Li, C.Z. Wu, *J. Alloys Compd* 1000 (2024) 175082.
- [56] L.W. Lu, H. Luo, G.X. Li, Y. Li, X.H. Wang, C.K. Huang, Z.Q. Lan, W.Z. Zhou, J. Guo, M. Ismail, H.Z. Liu, *Rare Metals* 43 (2024) 1153–1166.
- [57] V.V. Berezovets, R.V. Denys, I.Y. Zavaliv, Y.V. Kosarchyn, *Int. J. Hydrogen Energy* 47 (2022) 7289–7298.
- [58] G. Liu, L. Wang, Y. Hu, C. Sun, H. Leng, Q. Li, C. Wu, *J. Alloys Compd* 881 (2021) 160644.
- [59] Z.L. Ma, Q.K. Tang, J.L. Ni, Y.F. Zhu, Y. Zhang, H.W. Li, J.G. Zhang, Y.N. Liu, Z.X. Ba, L.Q. Li, *Chem. Eng. J.* 433 (2022) 134489.
- [60] H.W. Shang, W. Zhang, X. Wei, Y.Q. Li, Z.M. Yuan, J. Li, Y.H. Zhang, *J. Magnesium and Alloys* 12 (2024) 1593–1607.
- [61] H. Lu, J.B. Li, X. Zhou, Y.F. Lu, Y.A. Chen, Q. Li, F.S. Pan, *J. Mater. Sci. Technol.* 190 (2024) 135–144.
- [62] Z.L. Yuan, X.X. Zhang, Y.T. Wu, S.Y. Guan, S.Q. Zhao, L.Q. Ji, Q.M. Peng, S.M. Han, Y.P. Fan, B.Z. Liu, *J. Magnesium and Alloys* (2024) available online.